Structure-function analysis of RBP-J-interacting and tubulin-associated (RITA) reveals regions critical for repression of Notch target genes

Received for publication, April 17, 2017, and in revised form, May 4, 2017 Published, Papers in Press, May 9, 2017, DOI 10.1074/jbc.M117.791707

Nassif Tabaja[‡], Zhenyu Yuan[‡], Franz Oswald[§], and Rhett A. Kovall[‡1]

From the [‡]Department of Molecular Genetics, Biochemistry and Microbiology, University of Cincinnati College of Medicine, Cincinnati, Ohio 45267 and the [§]Department of Internal Medicine I, Center for Internal Medicine, University Medical Center Ulm, 89081 Ulm, Germany

Edited by Wolfgang Peti

The Notch pathway is a cell-to-cell signaling mechanism that is essential for tissue development and maintenance, and aberrant Notch signaling has been implicated in various cancers, congenital defects, and cardiovascular diseases. Notch signaling activates the expression of target genes, which are regulated by the transcription factor CSL (CBF1/RBP-J, Su(H), Lag-1). CSL interacts with both transcriptional corepressor and coactivator proteins, functioning as both a repressor and activator, respectively. Although Notch activation complexes are relatively well understood at the structural level, less is known about how CSL interacts with corepressors. Recently, a new RBP-J (mammalian CSL ortholog)-interacting protein termed RITA has been identified and shown to export RBP-J out of the nucleus, thereby leading to the down-regulation of Notch target gene expression. However, the molecular details of RBP-J/RITA interactions are unclear. Here, using a combination of biochemical/cellular, structural, and biophysical techniques, we demonstrate that endogenous RBP-J and RITA proteins interact in cells, map the binding regions necessary for RBP-J·RITA complex formation, and determine the X-ray structure of the RBP-J·RITA complex bound to DNA. To validate the structure and glean more insights into function, we tested structure-based RBP-J and RITA mutants with biochemical/cellular assays and isothermal titration calorimetry. Whereas our structural and biophysical studies demonstrate that RITA binds RBP-J similarly to the RAM (RBP-J-associated molecule) domain of Notch, our biochemical and cellular assays suggest that RITA interacts with additional regions in RBP-J. Taken together, these results provide molecular insights into the mechanism of RITA-mediated regulation of Notch signaling, contributing to our understanding of how CSL functions as a transcriptional repressor of Notch target genes.

Notch signaling is a highly conserved component of metazoan development and tissue homeostasis (1). Genetic ablation of Notch signaling is embryonic lethal (2). Furthermore, mutations leading to dysfunctional Notch signaling have been linked to certain types of cancers, cardiovascular disease, and birth defects, highlighting the importance of the Notch pathway in human disease (3, 4). Due to the negative human health outcomes associated with aberrant Notch signaling, there are ongoing efforts toward developing reagents that modulate Notch signaling to be used as potential therapeutics (5).

Notch is a juxtacrine signaling mechanism that is initiated when the extracellular domain of a DSL (Delta-like in mammals, Serrate in flies, LAG-2 in worms) ligand present on one cell binds a single-pass transmembrane Notch receptor on an adjacent cell (6) (Fig. 1*A*). In mammals, there are five DSL ligands (Jagged1 and -2 and Delta-like 1, 3, and 4) and four Notch receptors (Notch1–4) (6). Ligand/receptor interactions induce the Notch receptor to undergo a series of cleavage events, resulting in the release of the Notch intracellular domain (NICD)[2] from the cell membrane and its subsequent translocation to the nucleus (6). In the nucleus, NICD binds the transcription factor CSL (CBF1/RBP-J in mammals, Su(H) in flies, LAG-1 in worms) and the transcriptional coactivator MAM (Mastermind) (Fig. 1*B*) (7).

CSL has three domains that mediate contacts with coactivators and corepressors (Fig. 1, *C* and *D*): the N-terminal domain (NTD), the β-trefoil domain (BTD), and the C-terminal domain (CTD) (7). NICD contains an RBP-J-associated molecule (RAM) and an ankyrin repeat (ANK) domain that interacts with the BTD and CTD of CSL, respectively, which allow for MAM binding to the CTD and NTD (8–10). The CSL·NICD·MAM ternary complex binds enhancer and promoter elements of Notch target genes and functions as the switch to activate transcription at these sites (11). In the absence of a Notch signal, CSL functions as a transcriptional repressor by binding to corepressor proteins (11).

This work was supported by National Institutes of Health Grants 5R01CA178974 (to R. A. K.) and 5T32CA117846 (to N. T.). This work was further supported by German Research Foundation (DFG) Grant SFB1074/A3 and by the BMBF (Federal Ministry of Education and Research, research nucleus SyStAR) (to F. O.). The authors declare that they have no conflicts of interest with the contents of this article. The content is solely the responsibility of the authors and does not necessarily represent the official views of the National Institutes of Health.

The atomic coordinates and structure factors (code 5EG6) have been deposited in the Protein Data Bank (http://wwpdb.org/).

[1] To whom correspondence should be addressed. Tel.: 513-558-4631; Fax: 513-558-3512; E-mail: kovallra@ucmail.uc.edu.

[2] The abbreviations used are: NICD, Notch intracellular domain; ITC, isothermal titration calorimetry; NTD, N-terminal domain; BTD, β-trefoil domain; CTD, C-terminal domain; RAM, RBP-J-associated molecule; ANK, ankyrin repeat; SHARP, SMRT/HDAC-1-associated repressor protein; RBPID, RBP-J-interacting domain; NLS, nuclear localization signal; NES, nuclear export signal; aa, amino acids; MEF, mouse embryo fibroblast; WTP/AAA, WTP motif of RITA mutated to alanine; BisTris, 2-[bis(2-hydroxyethyl)amino]-2-(hydroxymethyl)propane-1,3-diol.

© 2017 by The American Society for Biochemistry and Molecular Biology, Inc. Published in the U.S.A.

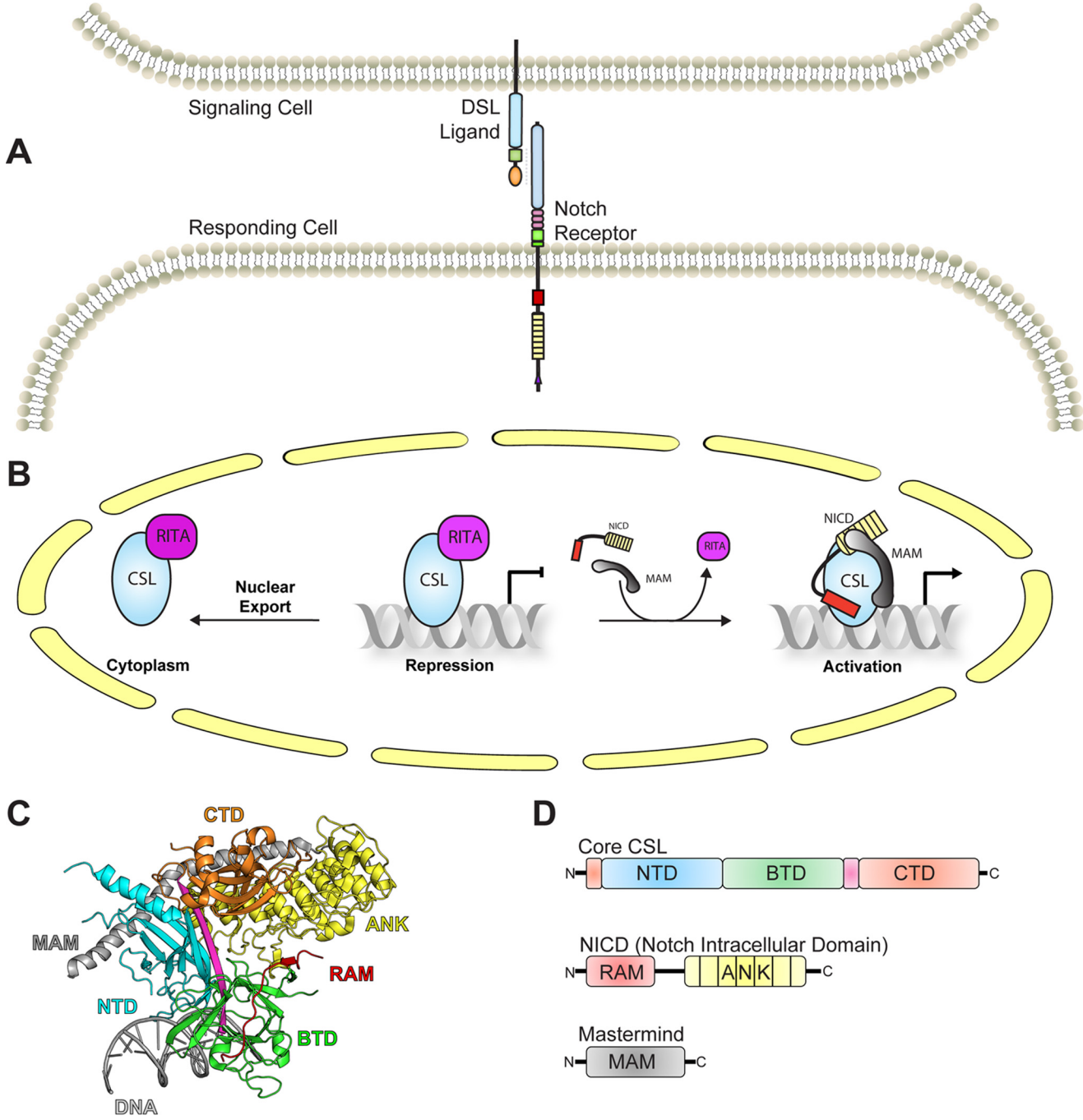

Figure 1. Overview of Notch signaling. *A*, Notch signaling occurs between neighboring cells, in which interactions on the cell surface between a Notch receptor and a DSL ligand result in cleavage of Notch and release of its intracellular domain (NICD), which subsequently transits to the nucleus. *B*, in the absence of a Notch signal, CSL can bind corepressors, such as RITA, to repress transcription from Notch target genes. RITA binding to CSL can also cause CSL to be exported out of the nucleus. Upon activation of the Notch signaling pathway, NICD and MAM (Mastermind) form a ternary complex with CSL that activates transcription from Notch target genes. *C*, structure of the CSL·NICD·MAM ternary complex bound to DNA (PDB entry 2FO1). The structural core of CSL is composed of three domains (NTD, BTD, and CTD), which are *colored cyan*, *green*, and *orange*, respectively. A β-strand that makes hydrogen-bonding interactions with all three domains is *colored magenta*. The RAM and ANK domains of NICD are *colored red* and *yellow*, respectively. MAM and DNA are *colored gray*. *D*, domain schematics are *colored* similarly to the structure.

When interacting with corepressors, such as KyoT2 (12), MINT (MSX-2-interacting nuclear target)/SHARP (SMRT/HDAC-1-associated repressor protein) (13, 14), or Hairless (15), the function of CSL is to anchor the assembly of higher-order repression complexes at Notch target gene sites. CSL·corepressor complexes often contain histone-modifying activity responsible for changing the local chromatin into a repressive environment (11). Early models in the field hypothesized that CSL was constitutively bound to DNA, and activation was a function of displacing corepressors with coactivators (16). However, more recent studies have demonstrated that CSL/DNA interactions *in vivo* are more dynamic, showing that CSL occupancy at target genes increases after activation of Notch signaling (17, 18). It remains inconclusive whether

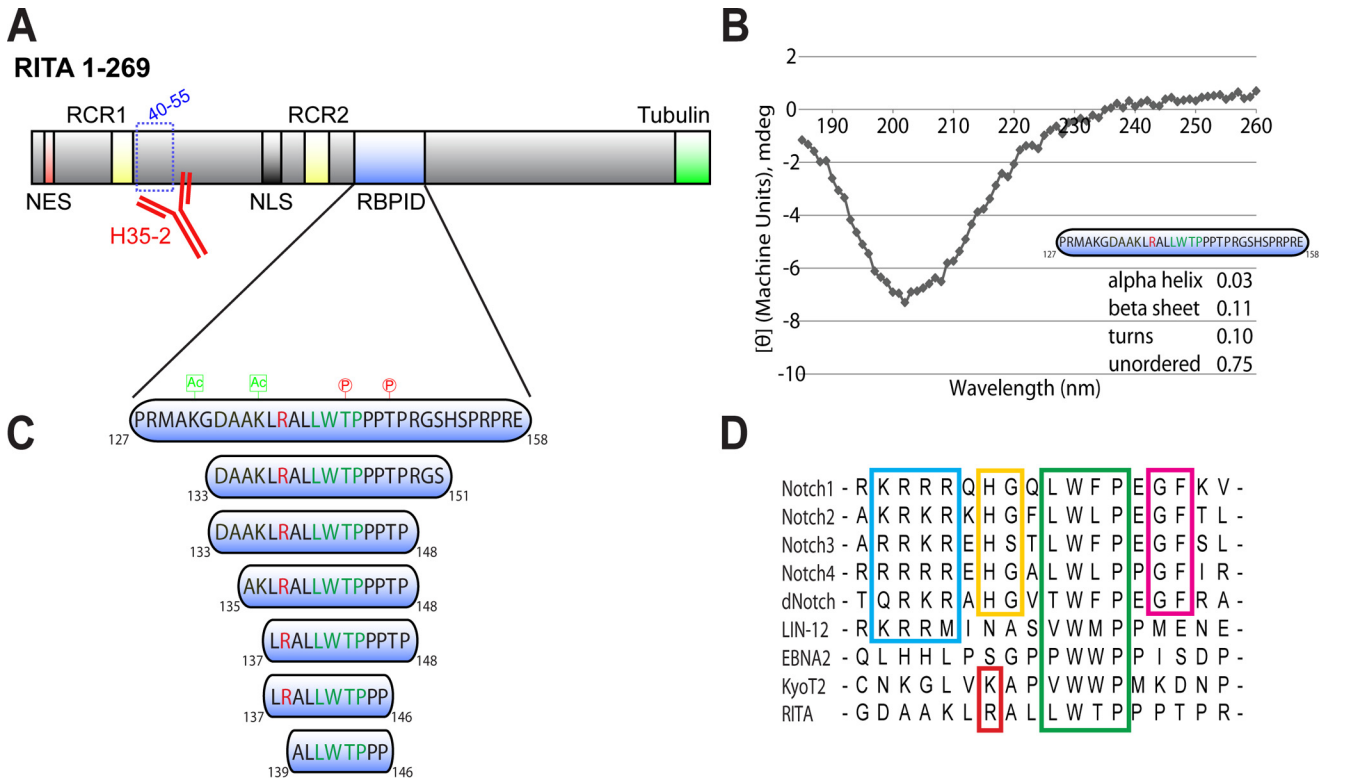

Figure 2. RITA domain schematic, secondary structure analysis, and sequence alignment with other CSL binding partners. *A*, RITA is a multidomain protein containing an N-terminal NES (*red*), RITA conserved repeats (RCR1/RCR2; *yellow*), NLS (*gray*), the RBPID (*blue*), and a C-terminal tubulin-interacting domain (*green*). As revealed by epitope mapping, the monoclonal antibody H35-2 (*red*) recognizes amino acids 40–55 of human RITA. *B*, far-UV CD spectra (wavelengths 185–200 nm) for the RBPID of RITA (amino acids 127–158). The RBPID consists of mostly random coil, as indicated by the minimum at 200 nm. Secondary structure was determined using Dichroweb and CDSSTR with reference set 7. The normalized root mean square deviation parameter value for the RITA CD data is 0.038. *C*, schematic representation of the RITA constructs used in this study with the φWφP motif *colored green* and the arginine implicated in salt-bridge formation with Glu-260 of RBP-J *colored red*. Previously identified post-translational modifications within the RBPID are shown; lysine acetylation sites are *colored green*, and threonine phosphorylation sites are *colored red*. *D*, sequence alignment of coregulators that bind the BTD of CSL, including the RAM domains of human Notch1–4, the RAM domains of fly (dNotch) and worm (LIN-12) Notch receptors, the viral coactivator EBNA2, and the corepressor KyoT2. *Boxed* in *blue*, the RAM basic motif; *boxed* in *yellow*, the HG dipeptide motif; *boxed* in *green*, the φWφP motif; *boxed* in *magenta*, the GF dipeptide motif; *boxed* in *red*, the basic residues of KyoT2 and RITA implicated in salt-bridge formation with RBP-J.

NICD is competing with corepressors for binding CSL molecules or if preassembled CSL transcriptional complexes are recruited to certain sites on DNA or if both modes are occurring simultaneously.

Structure-function studies of the Notch activator complex (CSL·NICD·MAM) have been seminal to understanding the transcriptional activation of Notch target genes (7); however, parallel structure-function studies of CSL·corepressor complexes and how CSL functions as a transcriptional repressor are lacking. Recently, a new transcriptional coregulator, termed RITA, has been identified from a yeast two-hybrid screen looking for RBP-J-binding partners (19). RITA is a 269-residue protein, which probably has little intrinsic secondary structure based on disorder prediction servers (Fig. 2, *A* and *B*). Proteomic studies have shown that RITA incurs numerous post-translational modifications in cells, including phosphorylation and acetylation (20, 21). Previously, a number of functional domains/regions have been mapped to RITA, including an RBP-J-interacting domain (RBPID), a nuclear localization signal (NLS), a nuclear export signal (NES), and a C-terminal tubulin-interacting domain (Fig. 2*A*) (19). As such, RITA has been shown to bind RBP-J and facilitate its export out of the nucleus (Fig. 1*B*) (19).

Previous studies have shown that RITA functions as a repressor of Notch-mediated transcription in cells as well as in *Xenopus* embryos, where it is able to reverse the loss of primary neurogenesis caused by Notch overactivation (19). Moreover, RITA overexpression has been shown to suppress growth and promote apoptosis in hepatocellular carcinoma (22). Although it is possible that this is due to repression of Notch target gene transcription, this remains to be determined.

The RBPID of RITA contains a conserved hydrophobic tetrapeptide motif (φWφP, where φ is any hydrophobic residue; Fig. 2*D*). This motif is also present in the RAM domain of Notch1–4, the corepressor KyoT2, and the viral proteins EBNA2 (Epstein-Barr virus nuclear antigen 2) and EBNA3C (Fig. 2*D*). The φWφP motif is critical for binding to the BTD of CSL (23, 24). The φWφP motif in RITA contains an atypical threonine (Thr-143) in the third position (Fig. 2*D*), and interestingly, Thr-143 has also been shown to be phosphorylated in cells (20). Three additional motifs have been identified in RAM that contribute to the high-affinity interaction with the BTD; these motifs consist of an N-terminal basic region and HG and GF dipeptide motifs (Fig. 2*D*) (25). However, these motifs are not present in other BTD binders, including RITA.

To deepen our understanding of the RBP-J·RITA corepressor complex, here we undertook a comprehensive structural, biophysical, and cellular characterization of RBP-J/RITA interactions. To this end, we determined the high-resolution X-ray structure of the RBP-J·RITA corepressor complex bound to DNA, defined the biochemical/cellular and thermodynamic interactions between RBP-J and RITA, analyzed how post-translational modifications in RITA affect these interactions, and began to characterize in cells how RITA acts to repress Notch target gene transcription. Taken together, our results provide molecular insights into RBP-J·RITA function, expanding our knowledge base of CSL·corepressor complexes.

Results

Endogenous RBP-J and RITA proteins interact in cells

Previous studies overexpressed RBP-J and RITA constructs in cultured cells to demonstrate biochemically that RBP-J interacts with RITA (19). To show that endogenous RBP-J and RITA proteins form a complex in cells, we generated a RITA-specific monoclonal antibody (H35-2; Fig. 2*A*). We first tested the H35-2 hybridoma supernatant using lysates from HeLa and HEK-293 cells. The antibody recognizes predominantly a protein of ~36 kDa, which is consistent with the calculated molecular mass of RITA (Fig. 3*A*). Next we tested lysates from several cell lines of epithelial and hematopoietic origin for RITA expression (Fig. 3*B*). Consistent with RITA mRNA being ubiquitously expressed *in vivo* (19), we detected RITA in all cell lines used. HEK-293, HeLa, and Jurkat cells exhibited the highest levels of RITA expression. RITA is also detected in A549, HEL-92.1.7, Kasumi-1, and SUP-T1 cells (Fig. 3*B*). Whereas there appears to be a dominant species of RITA in all of the cell lines tested, interestingly, various minor species of RITA appear in different cell lines, suggesting that RITA is post-translationally modified in a cell type-specific manner (Fig. 3*B*). To demonstrate that endogenous RBP-J and RITA proteins interact, we performed coimmunoprecipitation experiments using lysates from HeLa cells. As shown in Fig. 3*C*, endogenous RBP-J is coimmunoprecipitated only after RITA is immunoprecipitated with the anti-RITA supernatants H35-2, H35-1, or H35-9, but not with IgG alone.

Next, we sought to better define the regions of RITA that are required for interacting with RBP-J in cells (Fig. 4). We designed several deletion constructs of RITA (Fig. 4*A*) and transfected these GFP-RITA fusion constructs into HeLa cells. Fusion protein expression and subcellular location were confirmed using fluorescence microscopy (Fig. 4*B*). Subcellular localization of RITA proteins confirmed the previously identified NLS and tubulin-binding regions (19). As shown in Fig. 4*C*, endogenous RBP-J is co-immunoprecipitated with all GFP-RITA fusion protein constructs that contain the RBPID region, except for the construct that corresponds to RITA residues 120–161. Taken together, these data suggest that the RBPID region is required for the interaction with RBP-J in cells, but not sufficient, because other regions outside of the RBPID, such as RCR2, may also be involved in interactions with RBP-J *in vivo*.

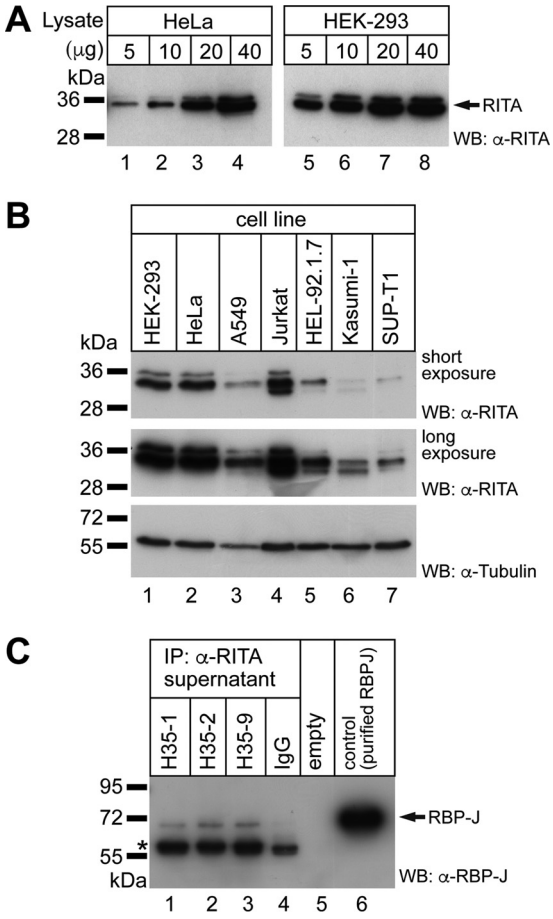

Figure 3. Endogenous RITA and RBP-J interact in cells. *A*, detection of endogenous RITA protein in HeLa cells (*left*) and HEK-293 cells (*right*). The indicated amounts of whole-cell lysates were used for Western blotting (*WB*). Membranes were incubated with the anti-RITA hybridoma supernatant H35-2. *B*, RITA expression levels in different human cell lines. Short exposure (top) and long exposure (*middle*) are shown. Expression of tubulin served as a loading control (*bottom*). Membranes were incubated with the anti-RITA hybridoma supernatant H35-2 (*top* and *middle*) or an anti-tubulin antibody (*bottom*). *C*, coimmunoprecipitations (*IP*) of endogenous RBP-J with RITA in HeLa cells. RBP-J was coimmunoprecipitated with RITA-specific hybridoma supernatants H35-1 (*lane 1*), H35-2 (*lane 2*), and H35-9 (*lane 3*) but not with an IgG control (*lane 4*). Purified RBP-J protein served as a positive control for Western blotting (*lane 6*). *, heavy chain of the antibodies.

Thermodynamic analysis of the requirements for RBP-J·RITA complex formation

Subsequently, we used ITC and CD with recombinant RBP-J·RITA proteins purified from bacteria to further analyze the binding interactions between RBP-J and RITA *in vitro* (Figs. 2*B* and 5 and Table 1). As shown in Fig. 5*A* and Table 1, a RITA construct (residues 106–173) that includes the RBPID and corresponds to the smallest construct in cells that interacts with RBP-J binds with a moderate ~1 μM K_d. For perspective, the affinity of RBP-J for RITA is 2 orders of magnitude weaker than the previously characterized NICD and KyoT2 interactions with RBP-J but comparable with interactions that the viral coactivator EBNA2 makes with RBP-J (25–27). The binding of RITA to RBP-J is enthalpically driven and incurs an entropic penalty (Table 1), which is consistent with RITA being an intrinsically disordered protein before interacting with RBP-J. We used far-UV CD to confirm that RITA is largely disordered in solution (Fig. 2*B*). The binding affinity of RITA to RBP-J is

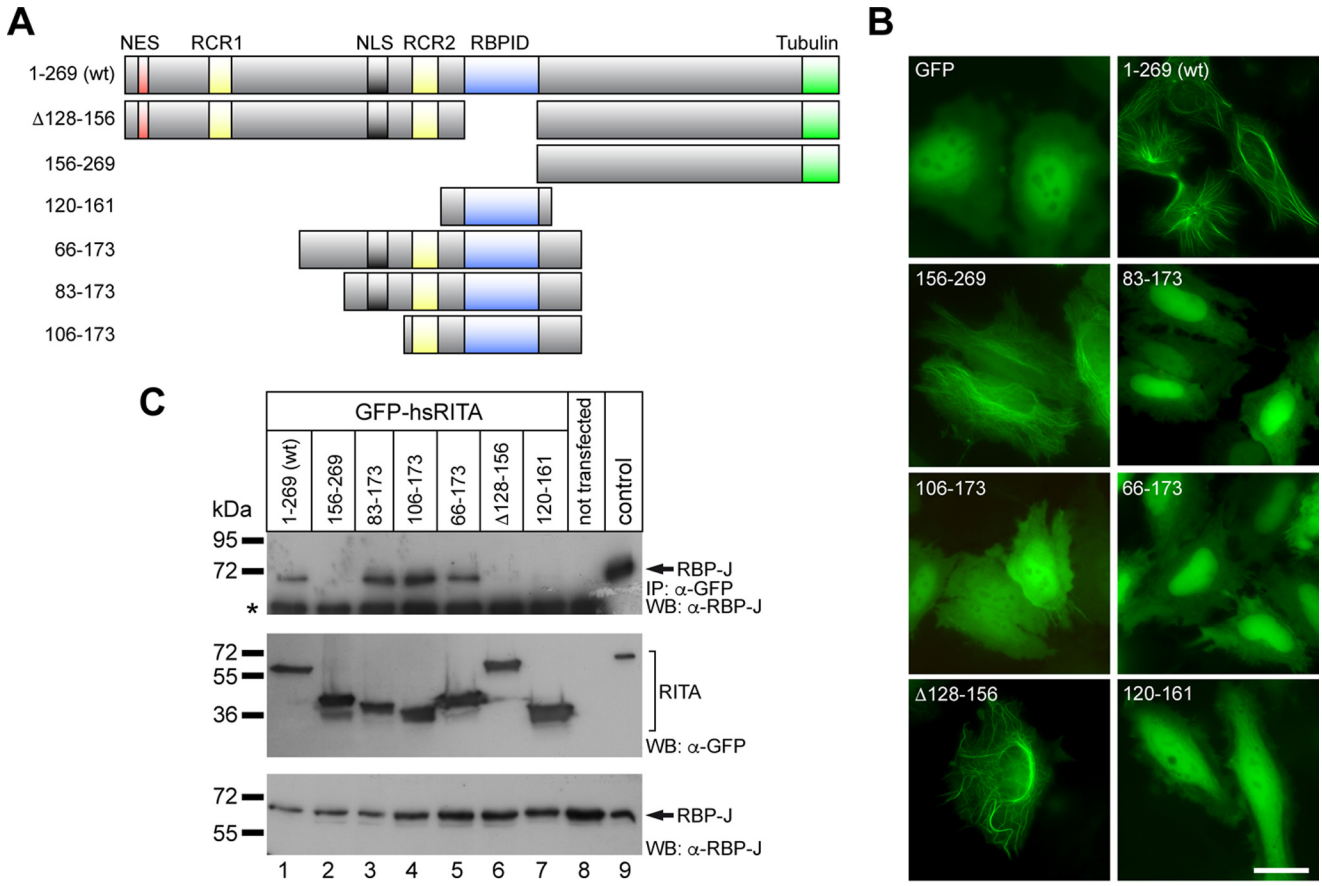

Figure 4. Mapping the minimal RBP-J binding region of RITA within cells. *A*, schematic representation of RITA deletion constructs used for analysis of subcellular localization and interactions with endogenous RBP-J. *Tubulin*, tubulin-binding region. *B*, subcellular localization of GFP-RITA fusion proteins used for coimmunoprecipitation experiments. RITA(WT) and RITA(Δ128–156) show predominant tubulin association due to their tubulin binding region and rapid nucleocytoplasmic shuttling (19). RITA(156–296) is also located at tubulin fibers, confirming the tubulin binding region at the C terminus of RITA. RITA(83–173) and RITA(66–173) show predominantly nuclear localization, confirming the NLS within RITA. RITA(120–161) and RITA(106–173) show equal distribution within the cell. GFP localization served as a control. HeLa cells were transfected with the indicated GFP fusion constructs. 24 h after transfection, the living cells were imaged by fluorescence microscopy. *Scale bar*, 10 μm. *C*, coimmunoprecipitations (*IP*) of RBP-J with RITA deletion constructions. *Top*, RBP-J interacts with RITA(WT) (*lane 1*), RITA(83–173) (*lane 3*), RITA(106–173) (*lane 4*), and RITA(66–173) (*lane 5*) but not with RITA(156–269) (*lane 2*), RITA(Δ128–165) (*lane 6*), and RITA(120–161) (*lane 7*). Expression of RITA proteins (*middle*) and endogenous RBP-J (*bottom*) was verified by Western blotting (*WB*). Coimmunoprecipitations were performed 24 h after transfection of the indicated GFP-RITA fusions. *, heavy chain of anti-GFP antibody used for immunoprecipitation of RITA proteins.

only marginally (<2-fold) increased by the presence of DNA containing a consensus CSL-binding site (Table 1). Similar to RBP-J interactions with other coregulators, such as RAM and KyoT2, there is a substantial (> 2 kcal/mol) favorable increase in the entropy of binding to RITA when RBP-J is prebound to DNA (Table 1) (26, 27).

To determine the region of RITA necessary and sufficient to bind RBP-J *in vitro*, we performed a series of ITC experiments with extended and serially truncated RITA constructs (Fig. 5 and Table 1). In contrast to our cellular/biochemical binding assays, RITA(127–158), which contains only the RBPID, binds RBP-J with similar affinity as the longer RITA construct (residues 106–173) (Fig. 5 (*A* and *B*) and Table 1). As shown in Table 1 and Fig. 5, further shortening of RITA (residues 133–151, 133–148, 135–148, 137–148, and 137–146) resulted in similar binding to RBP-J as RITA(127–158), except for RITA(139–146), which resulted in ~40-fold loss in binding affinity (Fig. 5*E* and Table 1). The isolated φWφP motif of RITA (LWTP) resulted in no binding to RBP-J (Table 1). These data suggest that RITA(137–148) encompasses the minimal region required to interact with RBP-J *in vitro*.

To define what domains of RBP-J interact with RITA, we performed ITC experiments with constructs that correspond to the BTD and BTD-CTD domains of RBP-J with RITA(127–158) (Fig. 5, *C* and *D*, and Table 1). Binding experiments performed with RITA and either the isolated BTD construct or the BTD-CTD construct showed similar binding as full-length core RBP-J. These data suggest that RITA binds the BTD of RBP-J.

To determine the change in heat capacity (ΔC_p) associated with RITA binding to RBP-J, we performed a series of ITC experiments, varying the temperature of the binding reaction. A negative ΔC_p is indicative of burial of nonpolar surfaces that occurs during protein complex formation (28). As shown in Fig. 5*F* and Table 2, the change in free energy, enthalpy, and entropy (ΔG^0, ΔH^0, $T\Delta S^0$) were analyzed as a function of temperature (5, 15, 25, and 35 °C). Whereas ΔG^0 is temperature-independent, ΔH^0 and ΔS^0 change with respect to temperature to maintain a constant ΔG^0. From this analysis, we determined that the ΔC_p associated with RBP-J/RITA interactions is −0.51 kcal/mol·K, which is similar to previously characterized CSL complexes, such as CSL·Kyot2 (ΔC_p = −0.57 kcal/mol·K) and CSL·RAM (ΔC_p = −0.62 kcal/mol·K) (26, 29), despite the

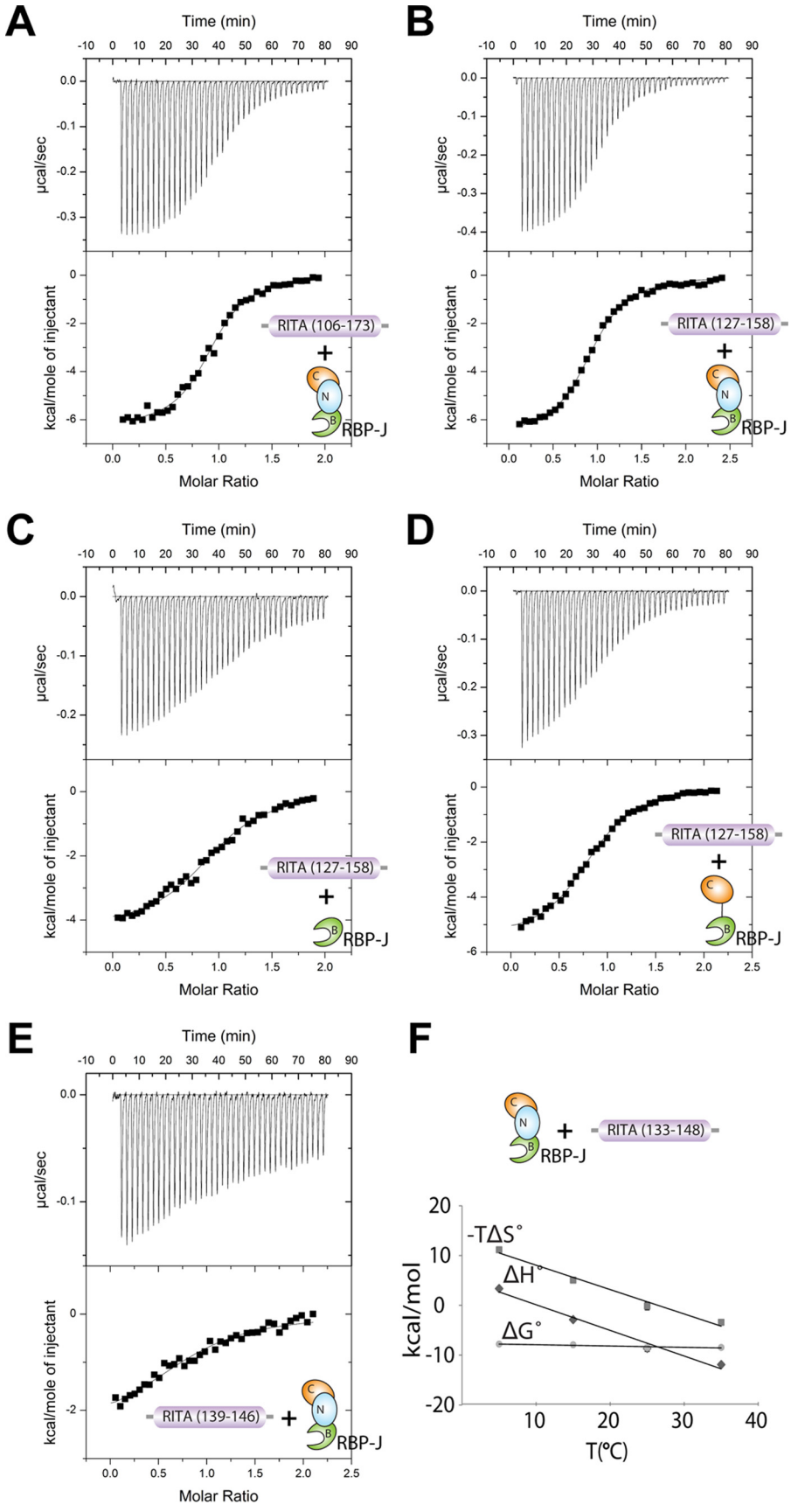
A
Time (min)
µcal/sec
kcal/mole of injectant
Molar Ratio
RITA (106-173)
RBP-J
B
Time (min)
µcal/sec
kcal/mole of injectant
Molar Ratio
RITA (127-158)
RBP-J
C
Time (min)
µcal/sec
kcal/mole of injectant
Molar Ratio
RITA (127-158)
RBP-J
D
Time (min)
µcal/sec
kcal/mole of injectant
Molar Ratio
RITA (127-158)
RBP-J
E
Time (min)
µcal/sec
kcal/mole of injectant
Molar Ratio
RITA (139-146)
RBP-J
F
RBP-J
RITA (133-148)
-TΔS°
ΔH°
ΔG°
kcal/mol
T(°C)

Table 1

Calorimetric data for RITA binding to RBP-J

All experiments were performed at 25 °C. Values are the mean of at least three independent experiments, and errors represent S.D. of multiple experiments. NBD, no binding detected.

RBP-J	RITA	K	K_d	ΔG^0	ΔH^0	$-T\Delta S^0$
	aa	M^{-1}	μM	*kcal/mol*	*kcal/mol*	*kcal/mol*
RBP-J	106–173	$1.1 \pm 0.2 \times 10^6$	0.98	-8.2 ± 0.1	-6.4 ± 0.7	-1.8 ± 0.9
RBP-J	127–158	$9.9 \pm 0.5 \times 10^6$	1.01	-8.2 ± 0.1	-6.1 ± 0.3	-2.1 ± 0.3
RBP-J + DNA	127–158	$1.7 \pm 0.2 \times 10^6$	0.59	-8.5 ± 0.1	-4.5 ± 0.1	-4.0 ± 0.2
BTD	127–158	$5.2 \pm 0.5 \times 10^5$	1.94	-7.8 ± 0.1	-4.0 ± 0.2	-3.8 ± 0.3
BTD-CTD	127–158	$5.8 \pm 0.2 \times 10^5$	1.71	-7.8 ± 0.1	-5.5 ± 0.1	-2.3 ± 0.1
RBP-J	133–151	$1.9 \pm 0.3 \times 10^6$	0.53	-8.5 ± 0.1	-7.6 ± 0.3	-0.9 ± 0.2
RBP-J	133–148	$2.1 \pm 0.3 \times 10^6$	0.49	-8.7 ± 0.1	-7.7 ± 0.3	-1.0 ± 0.4
RBP-J	135–148	$5.0 \pm 1.0 \times 10^6$	0.21	-9.1 ± 0.1	-6.7 ± 0.1	-2.4 ± 0.3
RBP-J	137–148	$2.0 \pm 0.1 \times 10^6$	0.50	-8.6 ± 0.1	-7.9 ± 0.1	-0.7 ± 0.1
RBP-J	137–146	$2.4 \pm 0.05 \times 10^6$	0.42	-8.7 ± 0.01	-8.5 ± 0.1	-0.1 ± 0.1
RBP-J	139–146	$2.4 \pm 0.3 \times 10^4$	43.2	-6.0 ± 0.1	-9.5 ± 0.8	3.5 ± 0.9
RBP-J	LWTP	NBD				

Table 2

Temperature dependence of RITA(133–148) binding to RBP-J

Values are the mean of three independent experiments, and the errors represent the S.D. of multiple experiments.

T	K	K_d	ΔG^0	ΔH^0	$-T\Delta S^0$
°C	M^{-1}	μM	*kcal/mol*	*kcal/mol*	*kcal/mol*
5	$4.0 \pm 0.3 \times 10^6$	0.43	-7.8 ± 0.2	3.3 ± 0.3	-11.1 ± 0.1
15	$1.1 \pm 0.3 \times 10^6$	1.0	-7.9 ± 0.2	-2.9 ± 0.1	-5.0 ± 0.3
25	$2.1 \pm 0.3 \times 10^6$	0.49	-8.7 ± 0.1	-7.7 ± 0.3	-1.0 ± 0.4
35	$1.0 \pm 0.4 \times 10^6$	1.0	-8.5 ± 0.1	-11.9 ± 0.1	3.4 ± 0.1

~100-fold weaker binding of RITA to RBP-J compared with these other coregulators.

Structure of the RBP-J·RITA·DNA complex

To determine the X-ray structure of the RBP-J·RITA complex bound to DNA (PDB entry 5EG6), we purified recombinant RBP-J (aa 53– 474) from bacteria and combined this with a RITA peptide corresponding to residues 133–151 and an oligomeric 15-mer DNA duplex, containing a single CSL-binding site. Using this complex to screen crystallization conditions resulted in an orthorhombic ($P2_122_1$) crystal form that diffracted to 2.1 Å resolution. Molecular replacement using published CSL·DNA structures was utilized to solve the RBP-J·RITA·DNA complex structure (27, 30). The asymmetric unit contains a single RBP-J·RITA complex bound to DNA (Fig. 6*A*). The final model consists of residues 53– 474 of RBP-J, residues 133–148 of RITA, and the 15-mer oligomeric DNA duplex, which was refined to an R_{work} and R_{free} of 19.3 and 23.6%, respectively (Table 3).

Overall, the fold of RBP-J in the context of the RBP-J·RITA·DNA complex largely conforms to that observed in previous CSL structures (Fig. 6*A*). However, one notable difference is observed in the CTD, whereby there is a rigid-body shift by as much as ~10 Å away from the BTD when compared with the structure of RBP-J·DNA (PDB entry 3IAG or 3BRG), resulting in a more open conformation (Fig. 6*B*). Although the significance of this unusual CTD confirmation remains to be determined, it should be mentioned that molecular dynamics simulations of the RBP-J·RITA·DNA complex suggest that the observed CTD conformation is a low-energy conformer and not a strained conformation (data not shown).

Consistent with our ITC binding studies, RITA binds exclusively to the BTD of RBP-J in an extended conformation (Fig. 6, *A* and *C*). A β-hairpin loop within the BTD forms a short antiparallel β-strand with N-terminal residues of RITA (aa 135–138) (Fig. 6, *A* and *C*). The φWφP motif of RITA (LWTP; aa 141–144) binds a nonpolar pocket on the surface of the BTD, and overall, the RBP-J/RITA interaction buries an estimated 987 $Å^2$ of surface area, similar to other BTD binders, such as the RAM domain of Notch (950 $Å^2$) and the corepressor KyoT2 (874 $Å^2$). Residues 133–148 of RITA had appreciable electron density, whereas the remaining three C-terminal residues were not well-resolved (Fig. 6*C*), which is consistent with our ITC binding studies that suggest these C-terminal residues contribute little to complex formation (Table 1).

Next, we compared the structure of RITA bound to RBP-J with the structures of RAM (PDB entries 3V79 and 3BRD) and KyoT2 (PDB entry 4J2X) bound to the BTD of RBP-J (Fig. 6*E*) (26, 27, 31). Overall, there is a large degree of structural correspondence between all of the structures, in particular in the region containing the φWφP motif, with more structural differences located at the N- and C-terminal residues of RITA, RAM, and KyoT2 (Fig. 6*E*). This is consistent with less sequence similarity for these proteins in this region (Fig. 2*D*). Interestingly, this structural comparison revealed that both RITA and KyoT2 form salt bridges with the BTD of RBP-J. In this case, Arg-138 of RITA and Lys-187 of KyoT2 form ionic interactions with the well-conserved residues Glu-259 and Glu-260 of RBP-J (Fig. 6*D*), providing a structural explanation for the conserved role of these residues in RBP-J. Consistent with the importance of this interaction in RBP-J·RITA complex formation and probably other BTD binders as well, disruption of the salt bridge by

Figure 5. Binding analysis of RBP-J/RITA interactions by ITC. Shown are representative thermograms from individual ITC experiments with various constructs of RBP-J and RITA. All ITC experiments were conducted with CSL in the cell at ~20–25 μM and RITA in the syringe at ~200–250 μM. Experimental temperature was set at 25 °C, and experiments were performed in triplicate ($n = 3$). *A*, a RITA construct (residues 106–173) that corresponds to the region necessary to interact with RBP-J binds with ~1 μM affinity. *B*, a RITA construct (residues 127–158) that corresponds to the RBPID also binds with ~1 μM affinity. *C* and *D*, the BTD and BTD-CTD constructs of RBP-J bind RITA(127–158) with ~2 μM affinity. *E*, further truncation of the RBPID (residues 139–146) results in a significant loss of binding to RBP-J. *F*, ΔC_p analysis of RBP-J/RITA interactions. ITC experiments were performed at 5, 15, 25, and 35 °C. The average change in Gibbs free energy (ΔG^0), enthalpy (ΔH^0), and entropy ($-T\Delta S^0$) were plotted as a function of temperature.

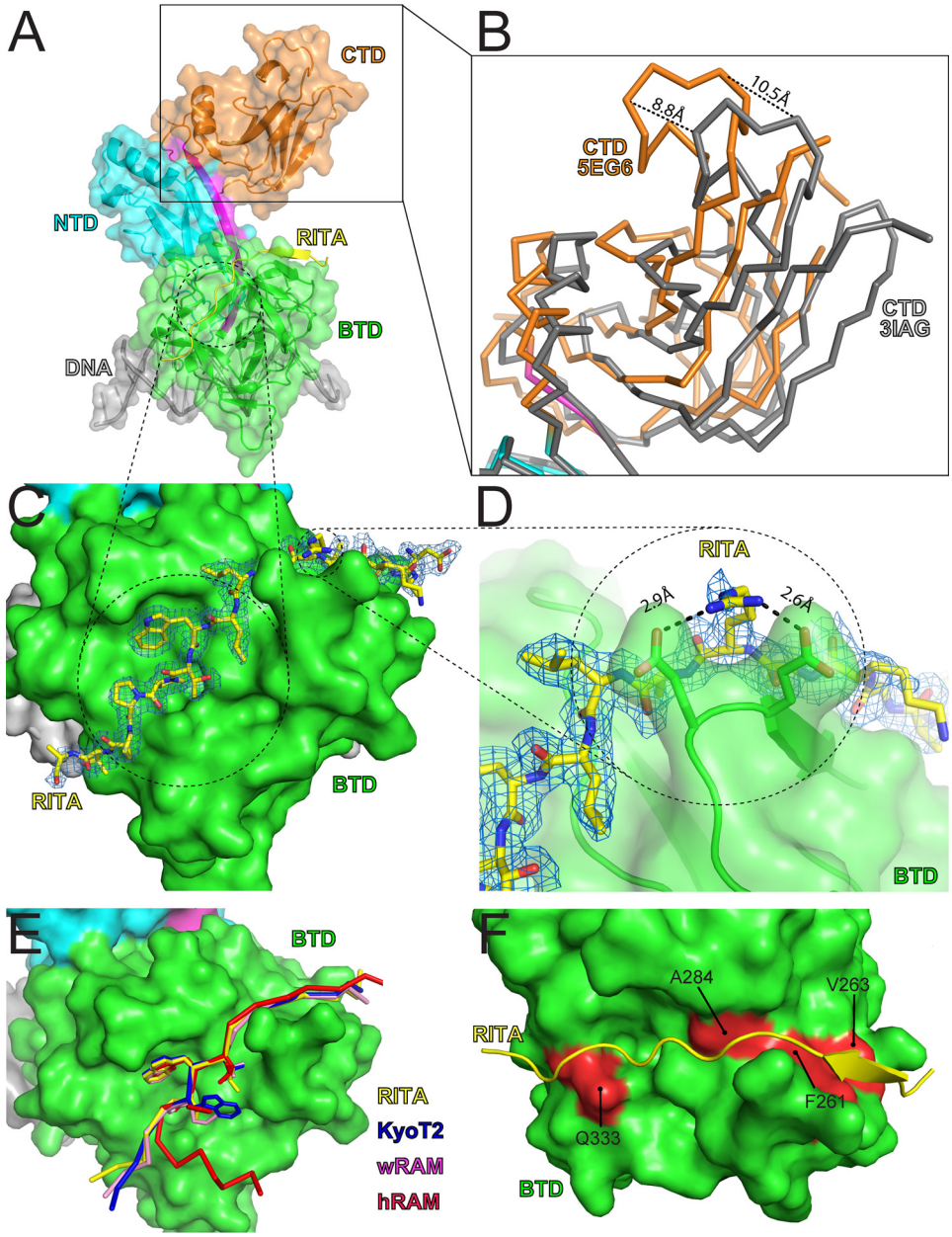

Figure 6. High-resolution structure of the RBP-J·RITA corepressor complex bound to DNA. *A*, the X-ray structure of RBP-J·RITA·DNA (PDB entry 5EG6) was determined to 2.1 Å resolution. Shown are a *ribbon* and *surface representation* of the complex structure with the NTD, BTD, and CTD *colored cyan*, *green*, and *orange*, respectively; RITA is *colored yellow*. *B*, structural overlay of CTD domains from the RBP-J·RITA·DNA structure determined here with the CTD from the previously published RBP-J/DNA structure (PDB entry 3IAG), highlighting the 10.5-Å rigid body shift of the CTD of RBP-J when bound to RITA. *C*, *enlarged view* of RITA binding the BTD of RBP-J, emphasizing the φWφP motif. RITA is shown in a *stick representation* with corresponding $2F_o - F_c$ electron density contoured at 1σ. *D*, salt bridge formed between Arg-138 of RITA (*yellow*) and Glu-259 and Glu-260 of RBP-J (*green*). *E*, structural alignment of BTD-binding proteins, including RITA in *yellow* (PDB entry 5EG6), KyoT2 in *blue* (PDB entry 42JX), worm RAM in *pink* (PDB entry 3BRD), and human RAM in *red* (PDB entry 3V79). Cα traces are shown with the side chains of the φWφP motifs depicted as *sticks*. *F*, location of the mutation sites (Phe-261, Val-263, Ala-284, and Gln-333) within the BTD that affect RAM binding and were used in this study.

mutation results in a ~30-fold ($\Delta\Delta G^0$ = 2 kcal/mol) loss of binding in ITC binding studies (Table 4).

Binding analysis of structure-based mutants

Given the similar binding mode of RITA and RAM for RBP-J, we analyzed the binding of RITA to RBP-J using a number of BTD mutants (Fig. 6*F*) that we previously showed affected RBP-J/RAM interactions (26, 32). All of these mutants had a dramatic effect on RAM binding to RBP-J, ranging from ~10- to 500-fold reductions in affinity (32). As shown in Table 4, BTD mutations at positions Phe-261 and Ala-284, which are near where the φWφP motif binds, had the largest effect on the affinity of RITA for RBP-J, ranging from ~10-fold reduction in binding (A284R) to no detectable binding by ITC (F261R). The BTD mutations at Val-263 and Gln-333, which interact with residues near the N and C termini of RITA, have a more modest effect on binding, ranging from a ~2- to 4-fold reduction in affinity. We also mutated the WTP motif of RITA (WTP/AAA), and as expected, no binding with RBP-J was detected (Table 4).

Table 3
Data collection and refinement statistics
Data for the highest-resolution shell are shown in parentheses. RMSD, root mean square deviation.

Data collection	
Beam line	APS LS-CAT 21-ID-F
Resolution (Å)	40.83 to 2.09 (2.15 to 2.09)
Space group	$P2_122_1$
Wavelength (Å)	0.97872
Unit cell: *a*, *b*, *c* (Å)	76.78, 96.41, 96.71
Unit cell: α, β, γ (degrees)	90.00, 90.00, 90.00
R_{merge}	0.07 (0.54)
$I/\sigma I$	22.8 (4.79)
Completeness (%)	89.6 (48.3)
Redundancy	7.1 (5.5)
Average mosaicity	0.46
Refinement	
R_{work}/R_{free} (%)	19.3/23.6
No. of reflections	38,486
No. of atoms	4285
Complexes/asymmetric unit	1
Wilson *B*/Mean *B* value (Å^2)	25.8/30.9
RMSD bond lengths (Å)	0.007
RMSD bond angles (degrees)	1.232
Ramachandran (favored/outliers) (%)	98.1/0.7

Proteomic studies have revealed that RITA is post-translationally modified in cells, and interestingly, a number of these modifications are contained within the RBPID of RITA (Fig. 2*C*) (20, 21). Therefore, we characterized the effect these modifications have on RBP-J·RITA binding, because these post-translational modifications may have a role in regulating this interaction. Previous studies have shown that RITA is phosphorylated on residues Thr-143 and Thr-147 and is acetylated on residues Lys-131 and Lys-136 (Fig. 2*C*) (20, 21). As shown in Table 5, phosphorylation of Thr-143, which resides within the φWφP motif of RITA, results in > 10-fold weaker binding ($\Delta\Delta G^0$ = 1.5 kcal/mol). In contrast, phosphorylation of Thr-147 of RITA, which in the structure is at the C terminus and is characterized by higher temperature factors, results in only a modest effect on binding (~2-fold; Table 5). Acetylation of Lys-131/Lys-136 of RITA results in ~5-fold weaker binding to RBP-J (Table 5), consistent with our structural data that show that these lysine residues are not making critical interactions with RBP-J (Fig. 6*C*).

Cellular characterization and validation of the RBP-J·RITA corepressor complex

We used transcriptional reporter assays to validate our RBP-J·RITA·DNA structure and further characterize RBP-J/RITA interactions in cells. To perform these studies, we used mouse embryonic fibroblasts (MEFs) derived from RBP-J null embryos and transduced these MEFs with retroviruses expressing either wild-type or mutant RBP-J proteins. A luciferase reporter that contains four RBP-J-binding sites (4×CBS) and a constitutively active form of the Notch1 receptor (NICD1) are cotransfected into the cells to monitor and activate Notch signaling (26, 32).

To demonstrate that RITA was functioning in our cultured MEFs similarly to previous studies (19), we transfected increasing amounts of RITA and analyzed the effect that it had on the Notch-activated reporter. As shown in Fig. 7*A*, RITA represses transcription from the reporter in a dose-dependent manner. Next, we analyzed the effects that the BTD mutants of RBP-J (F261A, V263A, A284V, and Q333A) had on the ability of RITA to repress activity from the transcriptional reporter in cells. It should be mentioned that these BTD mutants are inherently reduced for reporter activation due to the mutations affecting NICD binding to RBP-J (Fig. 7*B*) (26, 32). Thus, "relative activity" plotted on the *y* axis is represented relative to the maximal activity of that particular mutant and not the native protein (Fig. 7, *C–F*). Consistent with our binding studies and RBP-J·RITA structure, all four BTD mutants showed significantly less repression by RITA. These data suggest that the BTD mutations weaken the interactions between RBP-J and RITA in cells when compared with native RBP-J, thereby requiring higher levels of RITA expression to repress transcription from the reporter. However, somewhat contrary to our ITC binding studies, the F261A mutant only modestly affected RITA-mediated repression of the reporter, whereas Q333A had a stronger effect. These data suggest that regions outside the RBPID of RITA may be affecting interactions with RBP-J.

Finally, we tested several different RITA constructs in our cellular assays to address the importance of the RBPID and NLS/NES regions in mediating repression from the reporter in cells (Fig. 8). Consistent with previous studies (19), removal of either its nuclear export or import sequences results in a significant loss in the ability of RITA to repress transcription from the reporter (Fig. 8, *A* and *B*). Next, we transfected a RITA construct that corresponds to residues 106–173, which contains the RBPID but not the NES. In this case, similar repression was observed for the truncated construct compared with native full-length RITA, but statistically significant differences were observed at some amounts of transfected RITA (Fig. 8*C*). These data provide additional support that the NES of RITA and nuclear export of RBP-J are part of the RITA-mediated repression mechanism in cells. We also tested a full-length RITA construct, in which its WTP motif had been mutated to alanine (WTP/AAA; Fig. 8*D*). Interestingly, the WTP/AAA mutation severely affected the ability of RITA to repress activity from the reporter but did not completely abrogate it, supporting the hypothesis that regions outside the RBPID contribute to RBP-J/RITA interactions *in vivo*.

Discussion

Activation of the Notch signaling pathway results in transcription of target genes, mediated by the transcription factor CSL (1). This mechanism involves NICD and MAM binding CSL and recruiting additional coactivators and general transcription factors (11). CSL can also function as a repressor by binding to corepressors, such as MINT/SHARP, KyoT2, and RITA in mammals and Hairless in flies (13–15, 19). Understanding the molecular details of how coactivators and corepressors interact with CSL will be critical to building a detailed mechanistic model of the Notch pathway. Furthermore, knowledge gleaned from structure-function studies of CSL-mediated transcription complexes will inform and guide the discovery and design of reagents capable of modulating Notch signaling for therapeutic benefit.

Building upon prior structure-function studies of CSL·coregulator complexes, our work here comprehensively characterizes the interactions between RBP-J and the corepressor RITA both *in vitro* and in cells. We show that RITA is expressed

Table 4

Calorimetric binding data for RITA and RBP-J mutants

All experiments were performed at 25 °C. Values are the mean of at least three independent experiments, and errors represent the S.D. of multiple experiments. NBD, no binding detected.

RBP-J	RITA	K	K_d	ΔG^0	ΔH^0	$-T\Delta S^0$	$\Delta\Delta G^0$
		M^{-1}	μM	*kcal/mol*	*kcal/mol*	*kcal/mol*	*kcal/mol*
E259A/E260A	WT (135–148)	$1.7 \pm 1.0 \times 10^5$	6.21	-7.1 ± 0.1	-4.9 ± 0.6	-2.1 ± 0.7	2.0
F261R	WT (133–151)	NBD					
F261A	WT (133–151)	$6.9 \pm 1.0 \times 10^3$	147.2	-5.2 ± 0.1	-8.1 ± 0.8	2.9 ± 0.9	3.3
V263R	WT (133–151)	$0.9 \pm 0.2 \times 10^6$	1.29	-8.0 ± 0.2	-6.9 ± 0.6	-1.1 ± 0.8	0.5
V263A	WT (133–151)	$1.1 \pm 0.9 \times 10^6$	0.92	-8.1 ± 0.7	-5.9 ± 0.3	-3.0 ± 1.1	0.4
A284R	WT (133–151)	$1.8 \pm 0.4 \times 10^5$	5.88	-7.2 ± 0.1	-12.6 ± 1.1	5.5 ± 1.2	1.3
A284V	WT (133–151)	$4.6 \pm 0.8 \times 10^4$	21.9	-6.3 ± 0.1	-4.0 ± 0.9	-2.3 ± 1.0	2.2
Q333R	WT (133–151)	$4.8 \pm 0.3 \times 10^5$	2.1	-7.8 ± 0.1	-7.0 ± 0.3	-0.8 ± 0.3	0.7
Q333A	WT (133–151)	$1.2 \pm 0.3 \times 10^6$	0.90	-8.3 ± 0.1	-5.7 ± 0.2	-2.5 ± 0.3	0.2
WT	WTP/AAA	NBD					

Table 5

Calorimetric data for acetylated and phosphorylated RITA binding to RBP-J

All experiments were performed at 25 °C. Values are the mean of at least three independent experiments, and errors represent the S.D. of multiple experiments. pT143, Thr(P)-143; pT147, Thr(P)-147; acK131, acetylated Lys-131; acK136, acetylated Lys-136.

RBP-J	RITA	K	K_d	ΔG^0	ΔH^0	$-T\Delta S^0$	$\Delta\Delta G^0$
	aa	M^{-1}	μM	*kcal/mol*	*kcal/mol*	*kcal/mol*	*kcal/mol*
RBP-J	130–148	$1.1 \pm 0.2 \times 10^6$	0.90	-8.2 ± 0.1	-6.1 ± 0.4	-2.1 ± 0.3	
RBP-J	$130–148^{pT143}$	$8.6 \pm 0.1 \times 10^4$	12.0	-6.7 ± 0.1	-3.9 ± 0.4	-2.8 ± 0.5	1.5
RBP-J	$130–148^{pT147}$	$5.4 \pm 0.7 \times 10^5$	1.9	-7.8 ± 0.1	-5.3 ± 0.1	-2.5 ± 0.2	0.4
RBP-J	$130–148^{acK131/acK136}$	$1.9 \pm 0.4 \times 10^5$	5.0	-7.2 ± 0.1	-6.8 ± 0.2	-0.4 ± 0.2	1.0

in a variety of commonly used cell lines (Fig. 3*B*) and, importantly, that endogenous RBP-J and RITA proteins interact (Fig. 3*C*). Consistent with previous studies (19), we also show that RITA is a potent repressor of reporter activity in our transduced MEFs (Fig. 7*A*), which is dependent on both the NES and NLS of RITA (Fig. 8, *A* and *B*).

These studies prompted us to better define the regions in RITA that are required to interact with RBP-J in cells. We show that a region that includes the RBPID of RITA (*i.e.* the φWφP motif), which is essential for a number of coregulators to bind CSL, is necessary for interactions with RBP-J but, interestingly, not sufficient (Fig. 4*C*). Consistent with this result, a RITA construct, in which its φWφP motif has been mutated (WTP/AAA), still retains some activity in our transcriptional reporter assays (Fig. 8*D*). Conversely, our ITC studies of RBP-J·RITA complexes showed no differences in binding for RITA constructs that only contained the RBPID when compared with longer RITA constructs (Fig. 5 and Table 1). These data suggest that sequences outside of the RBPID contribute to RITA binding interactions with RBP-J *in vivo*. However, the nature of these upstream regions is unclear, but they may involve unidentified post-translational modifications of RITA and/or an additional binding partner. Conceivably, these additional interactions may involve the CTD of RBP-J, because previous studies have implicated the CTD in RBP-J/RITA interactions (33).

Nonetheless, we determined the 2.1 Å X-ray structure of the RBPID of RITA in complex with RBP-J and bound to DNA (Fig. 6 and Table 3). RITA binds the BTD of RBP-J in much the same way as the RAM domain of NICD and the corepressor KyoT2. However, RITA responds differently to BTD mutants that were designed to affect RBP-J/RAM interactions. On one hand, RBP-J/RITA interactions are drastically affected by mutations at Phe-261 and Ala-284, which interact with more central residues of the RBPID, including the φWφP motif, but on the other hand, RBP-J/RITA interactions are significantly less affected when compared with RAM by substitutions at Val-263 and Gln-333, RBP-J side chains that interact with RITA residues located more peripherally. Similar results with respect to the RBP-J mutants were observed in binding studies with KyoT2 (26); however, there are sequence differences in RITA and KyoT2 that discriminate their binding interactions with RBP-J as well. For example, the isolated KyoT2 φWφP motif (VWWP) weakly binds RBP-J with ~10 μM affinity (26), whereas the RITA φWφP motif (LWTP) does not (Fig. 2*D* and Table 1), and interestingly, the RITA 8-mer peptide (ALLWTPPP) binds ~20-fold more weakly than the corresponding KyoT2 peptide (APVWWPMK). Taken together, these data illustrate that different regions within coregulators that interact with BTD contribute different amounts of binding energy to achieve high-affinity interactions with RBP-J. This may allow for more flexibility in the types of sequences that can interact with the BTD of RBP-J.

Our structural studies also uncovered an unappreciated interaction between conserved residues in the BTD of RBP-J and RITA, which probably extends to all coregulators that bind the BTD of CSL. In this case, Arg-138 of RITA is flanked by Glu-259 and Glu-260 of RBP-J, making simultaneous ionic interactions with both glutamates. A similar interaction in the corepressor KyoT2, which involves a lysine instead of an arginine, is also observed in the context of the RBP-J·KyoT2·DNA complex structure (26). Alanine substitution at these sites (E259A/E260A) results in an unexpected 30-fold reduction in binding ($\Delta\Delta G^0 = 2$ kcal/mol), emphasizing the importance of this interaction. Previously, Johnson *et al.* (25) demonstrated the contribution of the conserved HG dipeptide motif from the RAM domain of Notch in interactions with RBP-J; however, the structural basis for this energetic contribution to binding was not understood. The histidine in the HG dipeptide motif of RAM corresponds to Arg-138 of RITA (Fig. 2*D*). It is interesting to speculate that a similar ionic interaction between this histi-

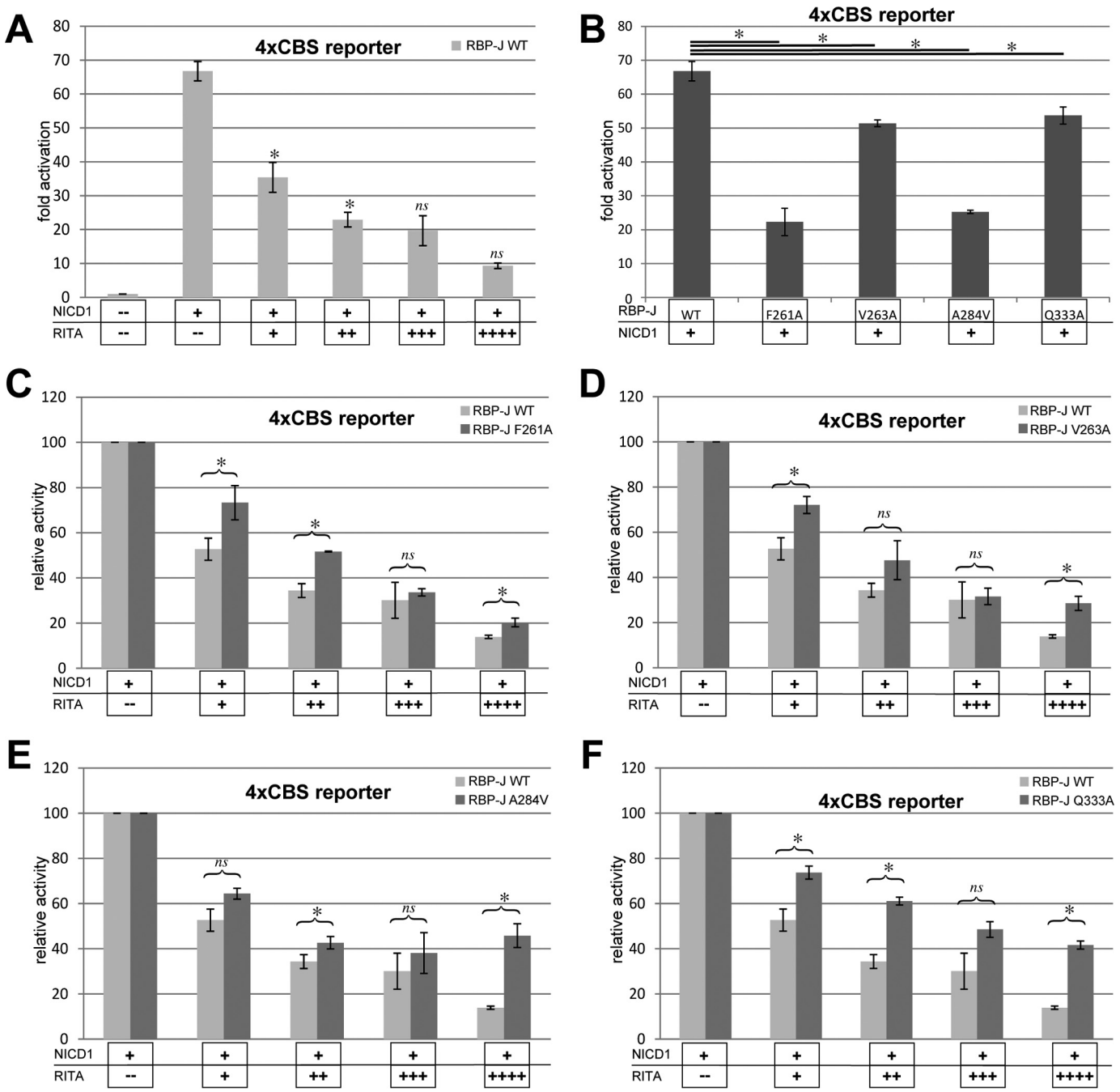

Figure 7. Cellular reporter assays of RITA-mediated repression in the context of CSL mutants. RBP-J null MEFs were transduced with a retrovirus encoding either wild-type or mutant RBP-J constructs. To activate and readout Notch signaling, cells were transfected with a construct that expresses an activated form of the Notch1 receptor (NICD1) and the 4×CBS reporter, which has four CSL-binding sites upstream of the firefly luciferase gene. To assay for RITA-mediated repression, cells were cotransfected with increasing amounts of a construct that expresses RITA: 0 ng (−), 50 ng (+), 100 ng (++), 200 ng (+++), or 400 ng (++++). Experiments were performed in triplicate, and the *error bars* represent S.E. *A*, RITA represses Notch reporter activity in a dose-dependent manner. -Fold activation is relative to luciferase activity from control cells not transfected with NICD1. *B*, plot shows reduced reporter activity for RBP-J mutants (F261A, V263A, A284V, and Q333A). -Fold activation is relative to luciferase activity from control cells not transfected with NICD1. *C–F*, plots show RITA-mediated repression for the RBP-J mutants compared with wild type. Data are normalized to cells with NICD1, but without RITA, and shown as relative activity. Statistical significance was determined by unpaired *t* test. *, $p \leq 0.05$; **, $p \leq 0.01$; *ns*, not significant.

dine in RAM and BTD residues Glu-259/Glu-260 of RBP-J occurs, which would provide a structural rationale for the importance of this interaction, albeit, the relatively low resolution structure of the human RBP-J·NICD·MAM·DNA complex that contains RAM does not support this interaction (31). Nonetheless, if this interaction occurs in solution, then the pK_a of the histidine may be perturbed to maintain its positive charge and ionic interactions with Glu-259/Glu-260. Future RBP-J·RAM studies that analyze binding as a function of pH may lend support to this hypothesis.

Finally, similar to other transcriptional coregulators, such as NICD, RITA incurs numerous post-translational modifications, including phosphorylation, acetylation, and methylation, and interestingly RITA is acetylated and phosphorylated within

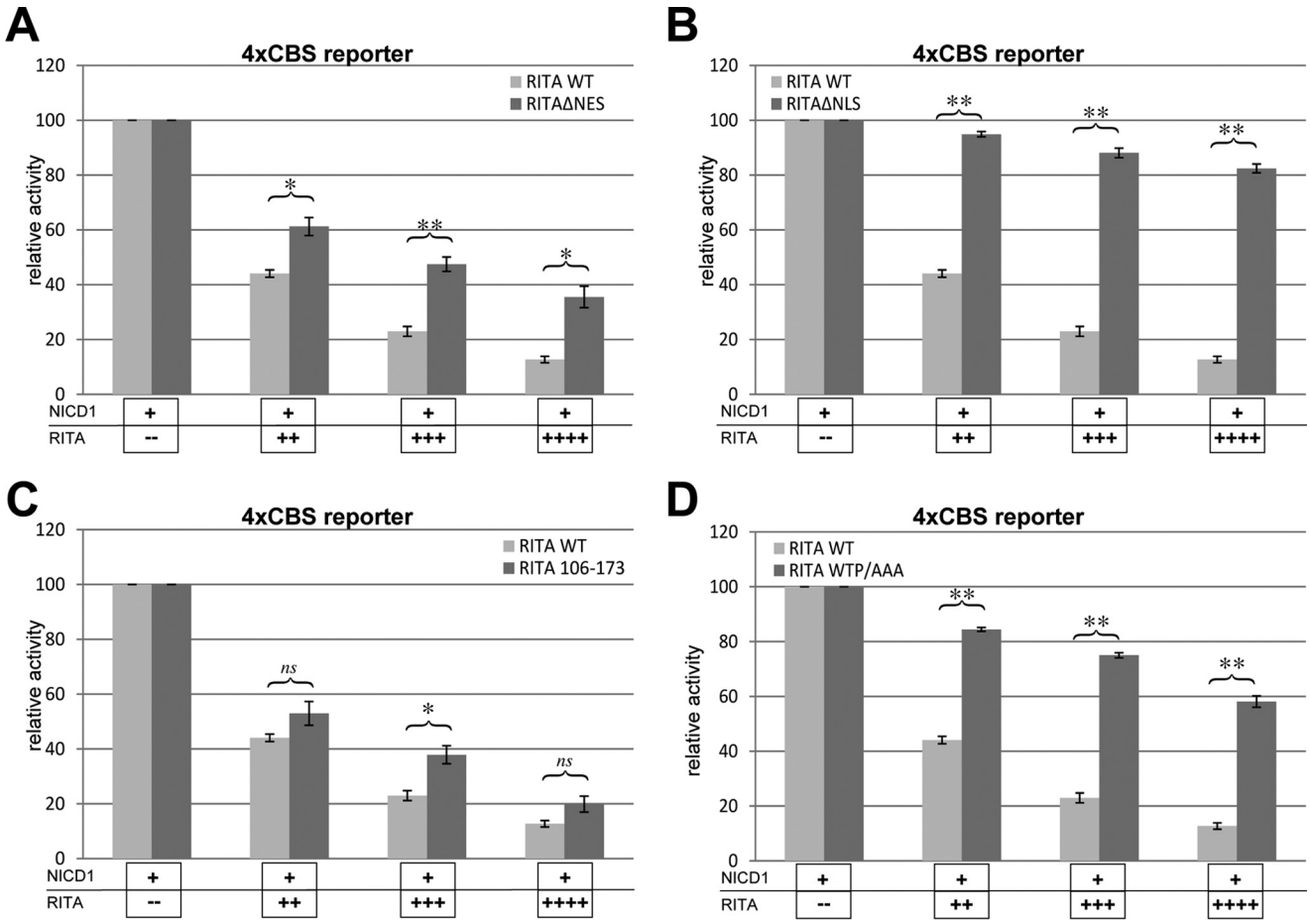

Figure 8. Cellular reporter assays of RITA-mediated repression in the context of RITA mutants. Cellular reporter assays in retrovirally transduced MEFs were performed similarly as described for Fig. 5. *A*, plot shows relative repression activity of RITA (residues 106–173), which contains the RBPID, compared with full-length RITA. *B*, plot shows reduced, but not completely abolished, RITA-mediated repression of the reporter for the RITA mutant WTP/AAA, which mutates the φWφP motif. *C*, plot shows reduced reporter activity, compared with wild type, for the construct RITAΔNES, which deletes the nuclear export sequence of RITA. *D*, plot shows reduced reporter activity, compared with wild type, for the construct RITAΔNLS, containing a non-functional NLS. *Error bars*, S.E. Statistical significance was determined by unpaired *t* test. *, $p \leq 0.05$; **, $p \leq 0.01$; *ns*, not significant.

its RBPID (20, 21). Moreover, the threonine (Thr-143) within the -WTP- motif of RITA is phosphorylated, a region that makes substantial contributions to binding RBP-J. Phosphorylation of Thr-143 (Thr(P)-143) results in a $>$ 10-fold loss in binding (Table 5). Given the other functions of RITA in the cell (*e.g.* tubulin binding), perhaps Thr(P)-143 is a mechanism to target RITA binding to RBP-J or tubulin within the cell, but not both simultaneously. Intriguingly, the viral transcriptional coregulator EBNA3C, which also interacts with RBP-J, contains a -WTP- motif and is involved in a myriad of virus-associated functions. Possibly, phosphorylation of the threonine in the -WTP- motif of EBNA3C is also involved in regulating RBP-J/EBNA3C interactions.

RITA is acetylated on lysine residues within its RBPID, but this modification only modestly affects binding to RBP-J. Interestingly, the RAM domain of Notch is also acetylated, albeit on different lysines. In this case, RAM acetylation leads to stabilization and increased half-life of NICD in the nucleus, whereas SIRT1 deacetylates NICD, leading to down-regulation of signaling. In future studies, it will be interesting to test whether RITA acetylation is also coupled to its half-life *in vivo*.

Experimental procedures

Cloning, expression, and protein purification

The *Mus musculus* CSL ortholog (RBP-J), residues 53–474 (CSL core domain), residues 203–393 (BTD), and residues 203–474 (BTD-CTD) were each cloned into the pGEX-6P-1 vector. Expression and purification were performed as described previously (30). Briefly, transformed bacteria were grown at 37 °C in LB medium, cooled to 20 °C, induced with 0.1 mM isopropyl β-D-thiogalactopyranoside, and grown overnight at 20 °C. The bacteria were harvested by centrifugation and resuspended in PBS. The resuspended cells were lysed by sonication, cleared by centrifugation and filtration, and subsequently loaded onto a glutathione-Sepharose column. The column was washed with PBS, and the GST-fusion protein was eluted using buffer containing reduced glutathione. The elutants were dialyzed, and the GST tag was cleaved with Precision Protease (GE Healthcare) per the manufacturer's protocol. All of the protein constructs were further purified to homogeneity using ion-exchange and size-exclusion chromatography.

The human RITA ortholog, residues 106–173 or residues 127–158, was cloned into a modified pET 28b(+) vector. This

vector encodes a fragment of SMT3 (suppressor of Mif2 temperature-sensitive mutant 3) for increased protein stability and expression, producing a His-SMT3-RITA fusion protein. The fusion protein was overexpressed as described above. The cleared lysate was incubated with nickel-nitrilotriacetic acid resin (Qiagen) and loaded into a gravity column. The column was washed, and fusion protein was eluted with imidazole-containing buffer. The fusion protein was then cleaved to remove His-SMT3 from the RITA moiety using the Ulp1 protease, which leaves only an N-terminal serine residue following cleavage. The RITA constructs were further purified to homogeneity using ion-exchange and size-exclusion chromatography. Constructs smaller than RITA(127–158) were purchased as HPLC-purified synthetic peptides from Peptide 2.0 and received as lyophilized powder.

Cell culture, immunoprecipitations, and Western blotting

The cell lines HEK-293 (ATCC number CRL1573) and A549 (ATCC number CCL-185) were grown in DMEM supplemented with 10% FCS, penicillin, and streptomycin. Kasumi-1 cells were grown in RPMI 1640, 20% FCS, 5% HEPES, 5% L-glutamine, penicillin, and streptomycin. Jurkat, HEL-92.1.7, and SUP-T1 cells were grown in RPMI 1640, 10% FCS, penicillin, and streptomycin. Expression vector pcDNA3-GFP-hsRITA and whole-cell lysates for Western blotting, immunoprecipitation, and immunostaining experiments were performed as described previously (19). The following antibodies were used: anti-RITA (H35-2, rabbit monoclonal IgG, generated commercially by Epitomics (Burlingame, CA); secondary antibody peroxidase-conjugated donkey anti-rabbit IgG, NA934V (GE Healthcare)), anti-tubulin (mouse monoclonal IgG, T9026 (Sigma-Aldrich); secondary antibody peroxidase-conjugated sheep anti-mouse IgG, NA931V (GE Healthcare)), anti-GFP (mouse monoclonal IgG, 7.1/13.1 (Roche Applied Science); secondary antibody NA931V (GE Healthcare)), anti-RBPJ (rat monoclonal IgG2a, T6709 (Cosmo Bio); secondary antibody peroxidase-conjugated goat anti-rat IgG, catalog no. 112-035-071 (Dianova)).

Fluorescence microscopy

HeLa cells were plated at a concentration of 1×10^5 cells/cm^2 on chamber coverslips (Nunc). After 16 h, cells were transfected with 300 ng of GFP or GFP-RITA expression plasmids using the Nanofectin transfection reagent (PAA Laboratories). 24 h after transfection, pictures were taken from living cells using a fluorescence microscope (IX71; Olympus) equipped with a digital camera (C4742; Hamamatsu) and a 100-W mercury lamp (HBO 103W/2; Osram). The following filter set was used for GFP detection: excitation, HQ470/40; emission, HQ525/50.

Isothermal titration calorimetry

ITC experiments were performed using a Microcal VP-ITC micocalorimeter. For all binding reactions, syringe concentrations varied between ~200 and 250 μM RITA, and cell concentrations varied between ~20 and 25 μM RBP-J. Titrations consisted of an initial 1-μl injection, followed by 39 7-μl injections. ITC binding experiments were performed in 50 mM sodium phosphate, pH 6.5, 150 mM NaCl at 5, 15, 25, or 35 °C. Samples were buffer-matched using size-exclusion chromatography. The collected data were analyzed using the ORIGIN software and fit to a one-site binding model.

Crystallization and data collection

A 15-mer DNA duplex (TTACTGTGGGAAAGA, AATCTTTCCCACAGT) with single-stranded TT/AA overhangs and containing a single CSL-binding site from the *HES-1* gene was co-crystallized with mouse CSL and human RITA. RBP-J·RITA·DNA complexes were set up in a 1:1.1:1.1 molar ratio and screened for crystallization conditions using the Hampton Research Index Screen and an Art Robbins Phoenix Crystallization Robot. The final optimized crystallization conditions were in a mother liquor containing 0.1 M BisTris, pH 5.5, 0.2 M ammonium acetate, 10% 1,4-butanediol, and 16% polyethylene glycol 3350. Crystals were grown at 4 °C using microbatch under paraffin oil methods, cryoprotected in mother liquor solutions containing 20% 1,4-butanediol, and flash-frozen in liquid nitrogen. The diffraction data were collected at the Advanced Photon Source (LS-CAT). The crystals diffracted to 2.1 Å and belong to the orthorhombic space group $P2_122_1$, with unit cell dimensions of 76.78, 96.41, and 96.71 Å.

Structure determination, model building, and refinement

Collected data were processed and scaled using HKL-2000 (34). Phaser was used to generate a molecular replacement solution (35), using the structure of mouse CSL bound to DNA (PDB entry 3IAG) as a search model (27). Coot was used to manually rebuild missing parts of the model (36). Translation/libration/screw parameters were calculated and used for refinement in Phenix Refine (37). Structural validation was performed using MolProbity (38). Our final model of the RBP-J·RITA complex bound to DNA consists of amino acids 53–474 of RBP-J, amino acids 133–148 of RITA, and the entire DNA duplex. The structure has been refined to an $R_{work} = 19.3\%$ and $R_{free} = 23.6\%$ and deposited in the PDB with code 5EG6 (39). We used the PyMOL Molecular Graphics System, version 1.3 (40), for structural visualization and alignments. The PDBePISA server (http://www.ebi.ac.uk/pdbe) was used to analyze protein-protein interfaces (41).

Cellular reporter assays

MEFs originating from RBP-J knock-out embryos (OT11) were transduced with retroviruses that express either wild-type or mutant RBP-J proteins, as described previously (32). Transduced MEFs were grown to 50% confluence in 6-well plates and transiently transfected with a constitutively active NICD1 construct, a 4×CBS luciferase reporter containing four CSL-binding sites, and *Renilla* luciferase construct (phRL). Wild-type or mutant RITA constructs were cotransfected in increasing concentrations to measure the repressive effects of RITA on Notch-mediated transcriptional activation of the luciferase reporter. *Trans*IT®-2020 transfection reagent (Mirus) was used for all transfections along with pBlueScript (Stratagene) to normalize the amount of DNA transfected in each experimental group. 48 h post-transfection, cells were harvested and prepared for measurement of firefly luciferase and *Renilla* lucifer-

ase activity. The Dual-Luciferase kit (Promega) was used to measure luciferase activity. For each experiment, firefly luciferase activity from the 4×CBS reporter was first normalized to *Renilla* luciferase activity. Normalized data were reported as either -fold activation or relative activity. Average values, errors, and S.D. were determined from at least three independent experiments performed in duplicate.

Circular dichroism

RITA(127–158) was characterized in a buffer containing 10 mM Tris-phosphoric acid, pH 7.4, and 50 mM NaF at a concentration of 384 μM (1.36 mg/ml). CD data were analyzed on DICHROWEB using the CDSSTR analysis program with reference set 7 (42, 43). CD measurements were taken in triplicate using an Aviv circular dichroism spectrometer model 215 at 25 °C in a 0.01-cm cuvette. Wavelength scans were performed between 185 and 290 nm using 1-nm increments.

Author contributions—R. A. K. and F. O. conceived of the study. R. A. K., N. T., Z. Y., and F. O. coordinated the research and contributed to data interpretation. N. T. and Z. Y. expressed and purified proteins, and N. T. solved the crystal structure of the RBP-J·RITA complex bound to DNA. N. T., Z. Y., and F. O. designed DNA constructs and conducted experiments. All authors wrote, edited, and approved the final draft of the manuscript.

Acknowledgments—We thank the Kovall and Oswald laboratories for technical assistance. This research used resources of the Advanced Photon Source, a United States Department of Energy (DOE) Office of Science User Facility operated for the DOE Office of Science by Argonne National Laboratory under Contract DE-AC02-06CH11357.

References

1. Bray, S. J. (2016) Notch signalling in context. *Nat. Rev. Mol. Cell Biol.* **17,** 722–735
2. Swiatek, P. J., Lindsell, C. E., del Amo, F. F., Weinmaster, G., and Gridley, T. (1994) Notch1 is essential for postimplantation development in mice. *Genes Dev.* **8,** 707–719
3. Gridley, T. (2003) Notch signaling and inherited disease syndromes. *Hum. Mol. Genet.* **12,** R9–R13
4. Koch, U., and Radtke, F. (2010) Notch signaling in solid tumors. *Curr. Top. Dev. Biol.* **92,** 411–455
5. Ntziachristos, P., Lim, J. S., Sage, J., and Aifantis, I. (2014) From fly wings to targeted cancer therapies: a centennial for notch signaling. *Cancer Cell* **25,** 318–334
6. Kopan, R., and Ilagan, M. X. (2009) The canonical Notch signaling pathway: unfolding the activation mechanism. *Cell* **137,** 216–233
7. Kovall, R. A., and Blacklow, S. C. (2010) Mechanistic insights into Notch receptor signaling from structural and biochemical studies. *Curr. Top. Dev. Biol.* **92,** 31–71
8. Wilson, J. J., and Kovall, R. A. (2006) Crystal structure of the CSL-Notch-Mastermind ternary complex bound to DNA. *Cell* **124,** 985–996
9. Nam, Y., Sliz, P., Song, L., Aster, J. C., and Blacklow, S. C. (2006) Structural basis for cooperativity in recruitment of MAML coactivators to Notch transcription complexes. *Cell* **124,** 973–983
10. Nam, Y., Weng, A. P., Aster, J. C., and Blacklow, S. C. (2003) Structural requirements for assembly of the CSL·intracellular Notch1·Mastermind-like 1 transcriptional activation complex. *J. Biol. Chem.* **278,** 21232–21239
11. Borggrefe, T., and Oswald, F. (2009) The Notch signaling pathway: transcriptional regulation at Notch target genes. *Cell Mol. Life Sci.* **66,** 1631–1646
12. Taniguchi, Y., Furukawa, T., Tun, T., Han, H., and Honjo, T. (1998) LIM protein KyoT2 negatively regulates transcription by association with the RBP-J DNA-binding protein. *Mol. Cell Biol.* **18,** 644–654
13. Kuroda, K., Han, H., Tani, S., Tanigaki, K., Tun, T., Furukawa, T., Taniguchi, Y., Kurooka, H., Hamada, Y., Toyokuni, S., and Honjo, T. (2003) Regulation of marginal zone B cell development by MINT, a suppressor of Notch/RBP-J signaling pathway. *Immunity* **18,** 301–312
14. Oswald, F., Kostezka, U., Astrahantseff, K., Bourteele, S., Dillinger, K., Zechner, U., Ludwig, L., Wilda, M., Hameister, H., Knöchel, W., Liptay, S., and Schmid, R. M. (2002) SHARP is a novel component of the Notch/RBP-Jκ signalling pathway. *EMBO J.* **21,** 5417–5426
15. Maier, D. (2006) Hairless: the ignored antagonist of the Notch signalling pathway. *Hereditas* **143,** 212–221
16. Hsieh, J. J., and Hayward, S. D. (1995) Masking of the CBF1/RBPJ κ transcriptional repression domain by Epstein-Barr virus EBNA2. *Science* **268,** 560–563
17. Krejcí, A., and Bray, S. (2007) Notch activation stimulates transient and selective binding of Su(H)/CSL to target enhancers. *Genes Dev.* **21,** 1322–1327
18. Castel, D., Mourikis, P., Bartels, S. J., Brinkman, A. B., Tajbakhsh, S., and Stunnenberg, H. G. (2013) Dynamic binding of RBPJ is determined by Notch signaling status. *Genes Dev.* **27,** 1059–1071
19. Wacker, S. A., Alvarado, C., von Wichert, G., Knippschild, U., Wiedenmann, J., Clauss, K., Nienhaus, G. U., Hameister, H., Baumann, B., Borggrefe, T., Knöchel, W., and Oswald, F. (2011) RITA, a novel modulator of Notch signalling, acts via nuclear export of RBP-J. *EMBO J.* **30,** 43–56
20. Kettenbach, A. N., Schweppe, D. K., Faherty, B. K., Pechenick, D., Pletnev, A. A., and Gerber, S. A. (2011) Quantitative phosphoproteomics identifies substrates and functional modules of Aurora and Polo-like kinase activities in mitotic cells. *Sci. Signal.* **4,** rs5
21. Li, X., Wang, W., Wang, J., Malovannaya, A., Xi, Y., Li, W., Guerra, R., Hawke, D. H., Qin, J., and Chen, J. (2015) Proteomic analyses reveal distinct chromatin-associated and soluble transcription factor complexes. *Mol. Syst. Biol.* **11,** 775
22. Wang, H., Chen, G., Wang, H., and Liu, C. (2013) RITA inhibits growth of human hepatocellular carcinoma through induction of apoptosis. *Oncol. Res.* **20,** 437–445
23. Tamura, K., Taniguchi, Y., Minoguchi, S., Sakai, T., Tun, T., Furukawa, T., and Honjo, T. (1995) Physical interaction between a novel domain of the receptor Notch and the transcription factor RBP-J κ/Su(H). *Curr. Biol.* **5,** 1416–1423
24. Ling, P. D., and Hayward, S. D. (1995) Contribution of conserved amino acids in mediating the interaction between EBNA2 and CBF1/RBPJk. *J. Virol.* **69,** 1944–1950
25. Johnson, S. E., Ilagan, M. X., Kopan, R., and Barrick, D. (2010) Thermodynamic analysis of the CSL × Notch interaction: distribution of binding energy of the Notch RAM region to the CSL β-trefoil domain and the mode of competition with the viral transactivator EBNA2. *J. Biol. Chem.* **285,** 6681–6692
26. Collins, K. J., Yuan, Z., and Kovall, R. A. (2014) Structure and function of the CSL-KyoT2 corepressor complex: a negative regulator of Notch signaling. *Structure* **22,** 70–81
27. Friedmann, D. R., Wilson, J. J., and Kovall, R. A. (2008) RAM-induced allostery facilitates assembly of a notch pathway active transcription complex. *J. Biol. Chem.* **283,** 14781–14791
28. Sturtevant, J. M. (1977) Heat capacity and entropy changes in processes involving proteins. *Proc. Natl. Acad. Sci. U.S.A.* **74,** 2236–2240
29. VanderWielen, B. D., Yuan, Z., Friedmann, D. R., and Kovall, R. A. (2011) Transcriptional repression in the Notch pathway: thermodynamic characterization of CSL-MINT (Msx2-interacting nuclear target protein) complexes. *J. Biol. Chem.* **286,** 14892–14902
30. Friedmann, D. R., and Kovall, R. A. (2010) Thermodynamic and structural insights into CSL-DNA complexes. *Protein Sci.* **19,** 34–46
31. Choi, S. H., Wales, T. E., Nam, Y., O'Donovan, D. J., Sliz, P., Engen, J. R., and Blacklow, S. C. (2012) Conformational locking upon cooperative assembly of notch transcription complexes. *Structure* **20,** 340–349
32. Yuan, Z., Friedmann, D. R., VanderWielen, B. D., Collins, K. J., and Kovall, R. A. (2012) Characterization of CSL (CBF-1, Su(H), Lag-1) mutants re-

veals differences in signaling mediated by Notch1 and Notch2. *J. Biol. Chem.* **287,** 34904–34916
33. Brockmann, B., Mastel, H., Oswald, F., and Maier, D. (2014) Analysis of the interaction between human RITA and *Drosophila* Suppressor of Hairless. *Hereditas* **151,** 209–219
34. Otwinowski, Z., and Minor, W. (1997) Processing of X-ray diffraction data collected in oscillation mode. *Methods Enzymol.* **276,** 307–326
35. McCoy, A. J., Grosse-Kunstleve, R. W., Adams, P. D., Winn, M. D., Storoni, L. C., and Read, R. J. (2007) Phaser crystallographic software. *J. Appl. Crystallogr.* **40,** 658–674
36. Emsley, P., and Cowtan, K. (2004) Coot: model-building tools for molecular graphics. *Acta Crystallogr. D Biol. Crystallogr.* **60,** 2126–2132
37. Adams, P. D., Afonine, P. V., Bunkóczi, G., Chen, V. B., Davis, I. W., Echols, N., Headd, J. J., Hung, L. W., Kapral, G. J., Grosse-Kunstleve, R. W., McCoy, A. J., Moriarty, N. W., Oeffner, R., Read, R. J., Richardson, D. C., *et al.* (2010) PHENIX: a comprehensive Python-based system for macromolecular structure solution. *Acta Crystallogr. D Biol. Crystallogr.* **66,** 213–221
38. Davis, I. W., Leaver-Fay, A., Chen, V. B., Block, J. N., Kapral, G. J., Wang, X., Murray, L. W., Arendall, W. B., 3rd, Snoeyink, J., Richardson, J. S., and Richardson, D. C. (2007) MolProbity: all-atom contacts and structure validation for proteins and nucleic acids. *Nucleic Acids Res.* **35,** W375–W383
39. Berman, H. M., Westbrook, J., Feng, Z., Gilliland, G., Bhat, T. N., Weissig, H., Shindyalov, I. N., and Bourne, P. E. (2000) The Protein Data Bank. *Nucleic Acids Res.* **28,** 235–242
40. DeLano, W. L. (2010) *The PyMOL Molecular Graphics System*, version 1.3r1, Schrodinger, LLC, New York
41. Krissinel, E., and Henrick, K. (2007) Inference of macromolecular assemblies from crystalline state. *J. Mol. Biol.* **372,** 774–797
42. Whitmore, L., and Wallace, B. A. (2004) DICHROWEB, an online server for protein secondary structure analyses from circular dichroism spectroscopic data. *Nucleic Acids Res.* **32,** W668–W673
43. Whitmore, L., and Wallace, B. A. (2008) Protein secondary structure analyses from circular dichroism spectroscopy: methods and reference databases. *Biopolymers* **89,** 392–400